

Track and energy reconstruction algorithms for time projection chamber with orthogonal fields

Martin Vavřík^{a,b} Babar Ali^b Hugo Natal da Luz^b Olivier Roussel^c Rudolf Sýkora^b Tomáš Sýkora^{a,b}

^a*Institute of Particle and Nuclear Physics, Faculty of Mathematics and Physics, Charles University, V Holešovičkách 2, 180 00 Prague 8, Czech Republic*

^b*Institute of Experimental and Applied Physics, Czech Technical University in Prague, Husova 5/240, 110 00 Prague 1, Czech Republic*

^c*Sorbonne Université, Université PSL, 75005 Paris, France*

E-mail: Martin.Vavrik@utef.cvut.cz

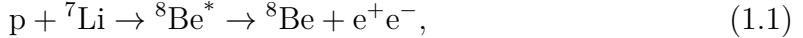
ABSTRACT: In this work, we describe the development of track- and energy-reconstruction algorithms for atypical Time Projection Chambers (TPCs) that will be used at the Institute of Experimental and Applied Physics, Czech Technical University in Prague, to search for the ATOMKI anomalous internal pair-creation phenomenon. These chambers operate with an inhomogeneous toroidal magnetic field oriented orthogonally to the electric field; we therefore refer to them as Orthogonal-Fields TPCs. Although this configuration distorts the drift inside the chamber and complicates the resulting electron and positron trajectories, it also offers several advantages. We present the most effective of several tested approaches, which employs a simulated ionization-electron drift map for track reconstruction and a Runge–Kutta–based fit for energy reconstruction. Finally, using simulations, we demonstrate that—assuming an ideal charge readout with no amplification and no noise, and with known initial track positions and directions—it is possible to achieve a fitted sigma better than 1% for both electrons and positrons after applying corrections for systematic effects dependent on track parameters.

Contents

1	Introduction	2
2	Experimental setup	4
2.1	Use of the VdG accelerator and general conception of the detector	4
2.2	Time projection chamber with orthogonal fields	5
3	Track and energy reconstruction algorithms for the OFTPC	7
3.1	Mapping of the drift	8
3.2	Simulation and reconstruction of primary tracks	11
3.3	Energy reconstruction	15
4	Update of 2D histogram of pair angle vs positron energy - angular uncertainty	17
5	Discussion of results and conclusion	18

1 Introduction

In 2015, the ATOMKI group (Hungary) observed in the decay of excited beryllium, produced in the process



an anomaly in the distribution of angle of positron-electron (e^+e^-) pairs [1], born by the standard Internal Pair Creation mechanism (IPC) [2].

Later, a similar anomalous behavior was also observed for other processes in which excited beryllium was replaced by helium ${}^4\text{He}$ nuclei (2019) [3] and carbon ${}^{12}\text{C}$ nuclei (2022) [4].

The observed anomaly has attracted wide attention, as it admits several beyond-standard-model explanations; for recent reviews, see, for example, [5, 6]. Several groups have announced their interest in similar measurements and are preparing corresponding detectors [7, 8] or have already performed measurements [9–11]. Nevertheless, no experiment other than ATOMKI (or linked to the ATOMKI group) has confirmed or disproved the observed anomaly yet.

The *shape* of the one-dimensional histogram produced by a detector with a very high (infinite) resolution would serve as convincing proof of the existence of a decaying particle, see Fig. 1.

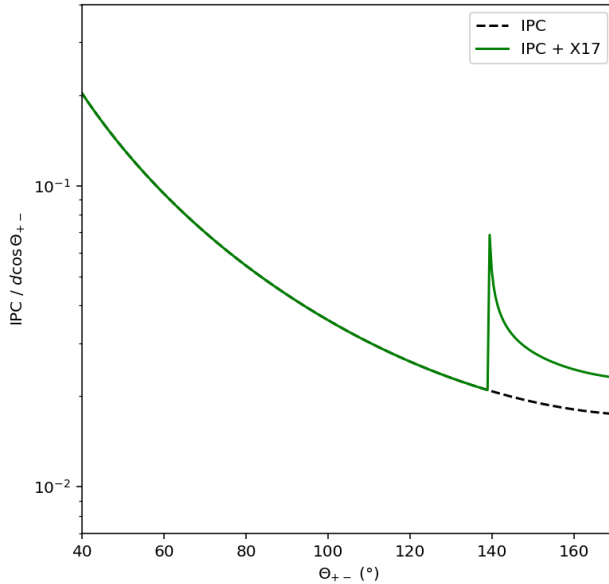


Figure 1: Angle θ between constituents of the e^+e^- pairs created for the combined IPC and X17 production, obtained by the analytical calculation. The branching ratio X17/IPC equal to 3×10^{-3} was used.

There is, however, no such detector, and the resolutions are limited. The real detector angular resolution affects the peak structure distribution and makes any conclusion about the *origin* of the peak, based on its shape, impossible.

On the other hand, the two-dimensional histogram correlating angle θ between the constituents of the e^+e^- pairs and positron energy, see Fig. 2, can be used due to the well-separated region (the separation gap) of decaying X17 particle from the background formed by the IPC.

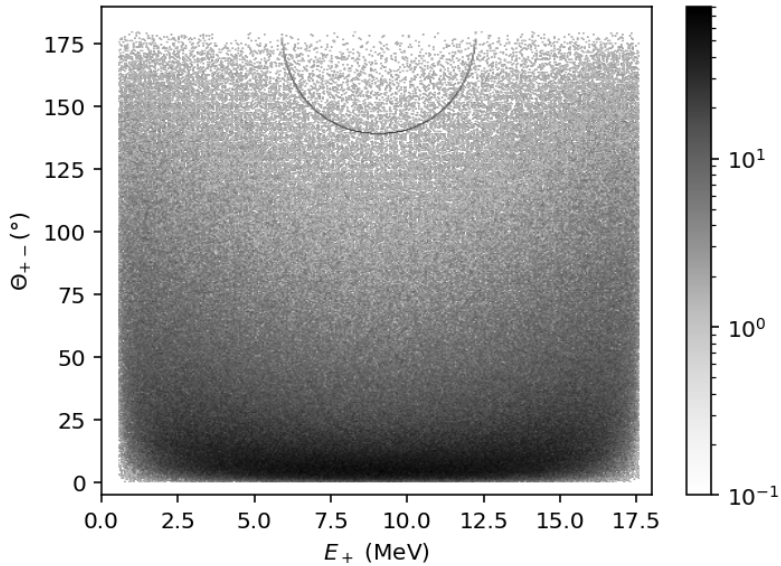


Figure 2: 2D histogram of pair angle vs positron energy created in the standard Internal Pair Creation process (here the mixture of transitions M1 + 0.21 E1 is considered), and pairs created by the decay of a hypothetical boson X17. The gap separating events from the decay production is clearly visible (here better on a linear scale). The data used for the plot come from a simulation; no detector effects influencing both the precision of angles and energies are included here, i.e., the true, generated values are plotted. To generate the plot, 1M events were used, which represents an expected lower bound on the number of to-be-measured events. The branching ratio X17/IPC equal to 3×10^{-3} was used.

Of course, both resolutions in angle θ and energy E must be reasonable to keep the signal well separated from the background. The current, technical, article is devoted to the algorithm used for the reconstruction of tracks and energies of charged particles in the non-standard, orthogonal field (OF), time projection chamber (TPC) used as a part of the apparatus for detection of the X17 object at the Van de Graaff (VdG) facility of the Institute of Experimental and Applied Physics of the Czech Technical University in Prague [12]. We leave, for a moment, the possibility to reconstruct

angles of tracks via the OFTPC open, as we rely on their reconstruction via Timepix3 detectors [13], see Fig. 3; however, we consider a comparison of reconstruction methods in the future.

The paper is organized as follows: first, the overall experimental setup is described, and then details of the construction of the time projection chamber with mutually orthogonal electric and magnetic fields, relevant for the reconstruction, are given. The track and energy reconstruction algorithms, representing the aim of the article, are described afterwards, together with their capabilities and limitations.

2 Experimental setup

2.1 Use of the VdG accelerator and general conception of the detector

Excited ${}^8\text{Be}$ nuclei, 17.64 or 18.15 MeV, are produced in collisions of protons accelerated by the VdG accelerator [12] to energies of 441 keV or 1.03 MeV with a thin disk-like target containing lithium.

Particles originating in the collision process, including e^+e^- pairs, are detected by three layers of detectors surrounding the target, see Fig. 3.

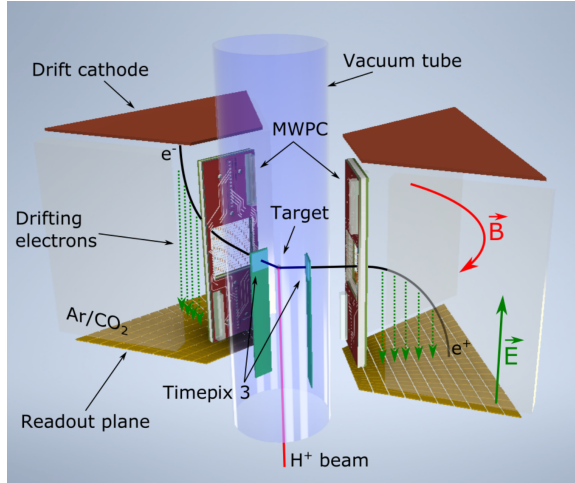


Figure 3: Schematics of OFTPC design, showing electric \vec{E} and magnetic \vec{B} fields and three layers of detectors: 1) Timepix3, for reconstruction of primary vertices origin vertices and particle tracks, 2) multi-wire proportional chambers (MWPC), providing information about the position of charged particles and direction of their momentum and 3) Time Projection Chambers, reconstructing the energy of each particle; read out pad plane is in bottom part here.

The first layer, see Fig. 3 (where only two of the six sectors are shown), consists of six Timepix3 (TPX3) detectors with their surfaces parallel to the beam. These detectors

serve for the reconstruction of e^+e^- origin vertices and the reconstruction of the angle between constituents of the e^+e^- pairs, for which we use the abbreviation θ_{+-} .

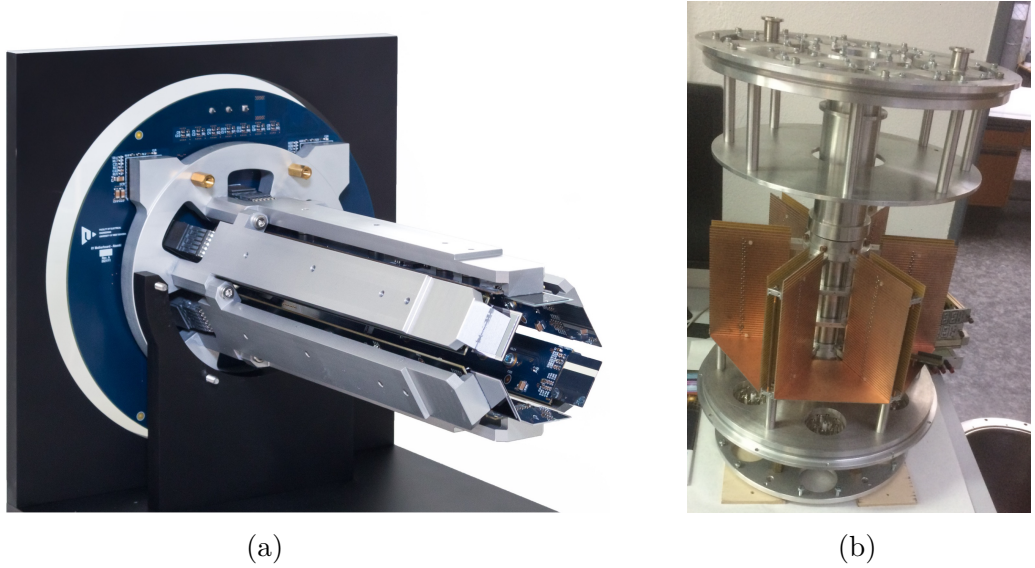


Figure 4: The Timepix3 hexagonal setup used in the measurements at the Van de Graaff accelerator, (a) the photography of the Timepix3 part, showing the target placed at the center, (b) the skeleton of the setup (compare with Fig. 3), showing the part of the beam pipe surrounded by magnets placed into a hexagonal structure (originally designed by the ATOMKI group). The part shown in (a) is inserted into the beam pipe shown in (b) from the bottom direction.

The second layer of detection consists of multi-wire proportional chambers (MWPC). Combining the position of the last hit pixel of the TPX3 with the MWPC position yields the direction information used later in the energy reconstruction.

Finally, the energy of each particle is reconstructed using the third layer, consisting of the six OFTPCs. The solution found for the final design of the TPC system, with orthogonal electric and magnetic field directions, considered the simplicity of the construction and the minimization of the electronic channels needed for the required value of energy resolution. Further technical details can be found in [13, 14].

The Timepix3 hexagonal setup to be used... The photograph shows no target at the center or anywhere. There are much better pictures of the TPC. It is standing on a table in the lab. Don't use this one. Remove "from the bottom direction"

2.2 Time projection chamber with orthogonal fields

Time projection chambers are used in many high-energy particle experiments, see e.g. [15, 16]. In their standard designs, the electric and magnetic fields are oriented parallel to each other. In such a case, there is no shift of the drift direction (Lorentz angle), the magnetic field may be increased as far as technically feasible, the gas pressure can be kept low, and the transverse diffusion of the electrons drifting in the gas is kept very small (see, e.g., [16], Section 11.7).

One of the most important challenges when designing and reconstructing data from TPCs is related to the effect caused by the non-zeroness of the vector product $\vec{E} \times \vec{B}$, and is usually linked to non-uniformities of the fields that, in some regions of the drift volume, lead to the existence of a component of magnetic field orthogonal to the electric field. The resulting force is no longer parallel to the electric field and generates distortions in the reconstructed trajectories. This effect compromises the accuracy of the determination of the energy of the particles.¹ However, the design does not always require parallelism of \vec{E} and \vec{B} fields; see designs of for example, CERES/NA45 [17], BONuS12 [18] and ALPHA-g [19] radial-drift TPCs.

For small TPCs, the distortions caused by the orthogonality of \vec{E} and \vec{B} fields are not as dramatic, as the secondary particles do not propagate over long distances. In fact, if the fields are assumed to be perpendicular from the beginning and corrections can be defined for the entire region, the effects of non-uniformity become less important. With that in mind, permanent magnets are used to generate a toroidal magnetic field. This results in a gas volume that is divided by the magnets into six independent segments. As the \vec{B} field bends the primary particles towards (positrons)/away from (electrons) the readout plane, their trajectories remain within the volume segment, together with all generated secondary particles. The high energy resolution of the OFTPC is achieved as a consequence of good timing resolution of the readout plane; in case of bending of primary particles along the readout plane, a much better (space) pixelization of the readout plane would be needed. The deviation of the secondary, i.e., drifting, electrons due to the magnetic field, in the end, is relatively small and allows performing reasonable corrections, as will be demonstrated later in this work. The gas mixture helps too — it can be shown, see e.g. Eq. 22 in [14], that selecting one with a lower drift velocity diminishes the distortions and improves the precision of the z-coordinate vertex position. The use of permanent magnets creating the magnetic field in a TPC volume is not unique, as other existing experiments show (e.g., the FASER [20] experiment uses a permanent magnet with a field intensity of 0.6 T). More details concerning the construction of the OFTPC are provided in [13, 14, 21].

Another reason for using permanent magnets is technical rather than economical. For a small experiment, it can be complicated (although not impossible) to generate a needed strong magnetic field (0.3 T) via an appropriate electromagnet, as such a spectrometer would require significantly more space.

When permanent magnets of a simple block shape are used, the simplest solution for a TPC module is shown in Fig. 3. This configuration results in mutually perpendicular

¹The $\vec{E} \times \vec{B}$ effect, see e.g. the Langevin approximation of the drift velocity vector in [15], varies as the angle between \vec{E} and \vec{B} changes on the particle trajectory. This means that the corrections (to the approximation) are dependent on position and can be, even for slight deviations, significant. Therefore, a very good knowledge of the critical regions of the detector and (eventually) space charge distortions is needed.

electric and magnetic fields throughout most of the volume, requiring only a limited amount of corrections at the boundaries of the magnets.

3 Track and energy reconstruction algorithms for the OFTPC

The background signal, e^+e^- pairs originating from the IPC process, is expected to be very significant, see Fig. 1. Therefore, proper reconstruction of the particle energy plays a key role in acquiring a clean sample well separated from the background.

Particles entering the OFTPC volume are denoted as primary ones and those produced within the volume as secondaries. Any primary particle of interest, i.e., an electron or positron from a e^+e^- pair, is relativistic. Therefore, its movement within the OFTPC volume is not significantly (measurably) affected by its interaction with the gas filling the OFTPC volume, and its trajectory is then ruled by the Lorentz force. The electric field \vec{E} is considered to be uniform in the OFTPC volume; the non-uniform magnetic field \vec{B} is given by the superposition of the magnetic fields of permanent magnets. In the first approximation, both fields are considered ideal (as calculated by finite element methods), and their values are defined at the 3D space grid points. Later, the ideal values will be replaced by the measured values.

Energy reconstruction, along with its testing on simulations, requires three steps:

1. **Mapping of the drift:** In a TPC with an ideal (continuous) readout, each secondary electron produced by an interaction of the primary particle at the coordinates (x, y, z) is registered on the readout as (x', y', t) , see Fig. 5. Since the drift path of the secondary electrons is distorted by the $\vec{E} \times \vec{B}$ effect, we cannot simply assume a direct correspondence between these coordinates, i.e., $(x, y, z) \neq (x', y', v_d t)$, where v_d is the drift velocity. Therefore, a mapping \mathcal{M} between the two spaces must be determined. To get an approximation of the mapping, the drift of a large number of electrons from known initial positions covering the detector volume towards the readout was simulated. The process of charge multiplication via a Gas Electron Multiplier (GEM; located at the position of the readout plane) is neglected here.
2. **Simulation and reconstruction of primary tracks:** Primary electron and positron tracks entering the detector were simulated, as well as the drift of the secondary electrons generated by the interactions with the gas. The positions of the interactions along the track were reconstructed in the form of track voxels from the detector data (charge $q(x_{\text{pad}}, y_{\text{pad}}, t)$ in each pad and time bin) using the map determined in the previous step.
3. **Energy reconstruction:** Based on the set of reconstructed positions of interaction along the track (in the form of voxels with charge information), the

particle (electron or positron) track is fitted using the energy of the particle as the parameter.

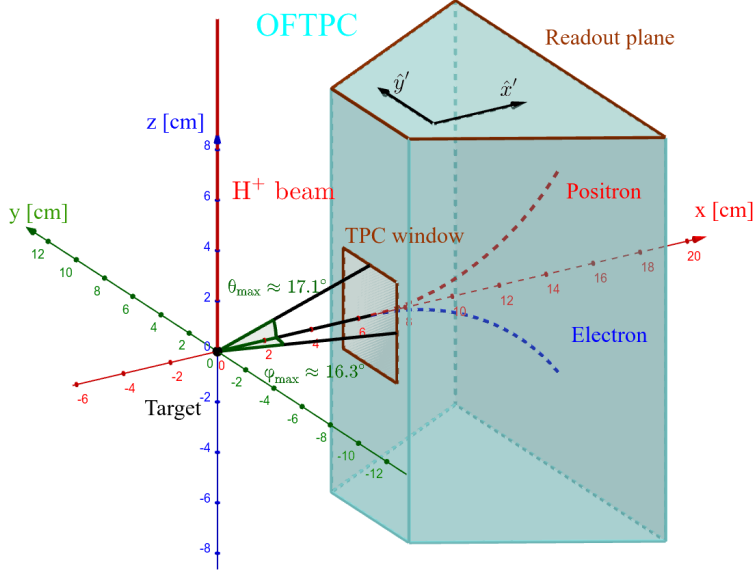


Figure 5: The coordinate systems and the OFTPC detector: (x, y, z) coordinates are used for the description of the full detector (and tracks), coordinates (x', y', t) for the pad plane. The positions of the beam, target, and window as well as the position and coordinates of the readout plane are shown. The spherical angles θ and φ (taken from the equator plane xy) are used to describe the particle momentum direction. Made with GeoGebra®.

The MWPC and TPX3 detector layers provide boundary conditions for each track: the position of a charged particle entering the volume of the OFTPC is measured by the MWPC (with a precision of $500\text{ }\mu\text{m}$), the direction of the particle momentum vector on its entrance to the OFTPC can be estimated using the last TPX3 pixel (its size is $50\text{ }\mu\text{m} \times 50\text{ }\mu\text{m}$), and the position measured by the MWPC. In this paper, we assume that these conditions will be known exactly; in the future, they may be further refined in a fit.

3.1 Mapping of the drift

To account for the drift distortion by the magnetic field, a simulation is needed for the reconstruction procedure — the first step is to get a (direct) mapping from the detector space \mathcal{D} to the readout space \mathcal{R}

$$\overline{\mathcal{M}}: \mathcal{D} \rightarrow \mathcal{R}, (x, y, z) \mapsto (\bar{x}', \bar{y}', \bar{t}) \quad (3.1)$$

of the average readout coordinates (position on the readout plane \bar{x}', \bar{y}' and drift time \bar{t}) corresponding to the ionization vertices (x, y, z) inside the OFTPC.

For the drift movement of secondaries (and eventually the development of avalanches) in the OFTPC, we use the Garfield++ toolkit [22]. Garfield++ serves for the detailed simulation of gas and semiconductor particle detectors via ionization. There are two basic options for ionization electrons in Garfield++:

1. **AvalancheMC** (Avalanche Monte Carlo) tracking, which requires a gas table calculation and applies a random diffusion step using precalculated coefficients,
2. **AvalancheMicroscopic** tracking, which uses the equation of motion to follow electrons from collision to collision and models scattering.

The latter is generally slower but more precise, especially for small structures. It was used in this work because, having tilted/curved drift trajectories due to the magnetic field, see Fig. 9, we get all the details about drifting secondaries.

The (direct) mapping is created using the microscopic simulation of the motion of secondary electrons. The initial positions of these electrons are determined by a regular (Cartesian) grid in the detector space (x, y, z) , and the initial velocity is close to zero (in comparison with the average for such electrons in a track, but still faster than the drift velocity) in a random direction. We simulate $n = 100$ ionization electrons at each point of the regular grid inside the OFTPC and average their readout coordinates:

$$\overline{\mathcal{M}}: \mathcal{D} \rightarrow \mathcal{R}, (x, y, z) \mapsto \frac{1}{n} \sum_{i=1}^n (x'_i, y'_i, t_i). \quad (3.2)$$

For the visualization of such a simulation, see Fig. 6 and Fig. 7 for visualization of the results. We also obtain information about the distribution of these readout positions due to the randomness of electron collisions with gas particles.² We can create a continuous map by using trilinear interpolation within the regular grid.

The inverse map $\overline{\mathcal{M}}^{-1}$ is made as a combination of the exact map (in grid points) and an appropriate interpolation between these points, with the possible consequence that $\overline{\mathcal{M}}$ and $\overline{\mathcal{M}}^{-1}$ are not perfectly inverse to each other outside the simulated grid points. In the end, the difference should be negligible.

We tested two methods of inversion — polynomial interpolation in the irregular grid in the readout space (main, faster method), and trilinear interpolation in the regular grid combined with gradient descent search for inversion (slower, but better in some extreme cases near the poles of the magnets, see Fig. 8). In the first method, we use a binary search algorithm [24] to find the eight grid points that surround³

²From preliminary tests (e.g., Mardia's test of skewness and kurtosis [23]), we see that the distribution of readout positions of ionization electrons caused by diffusion is well-described by a multivariate normal distribution. This information can be used to speed up the track simulation with Monte Carlo.

³This is non-trivial, since these points alone do not define a closed volume; instead, we require that each of the points' coordinates lies between the minimum and maximum of corresponding coordinates of the eight points.

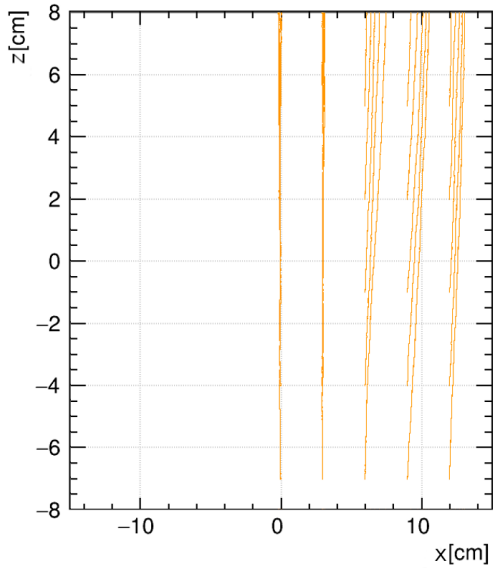


Figure 6: An example of a simulation of the mapping \mathcal{M} , showing how regular grid (x, y, z) points are mapped to readout plane coordinates and providing a base for understanding the resulting irregularity of (x', y', t) grid points.

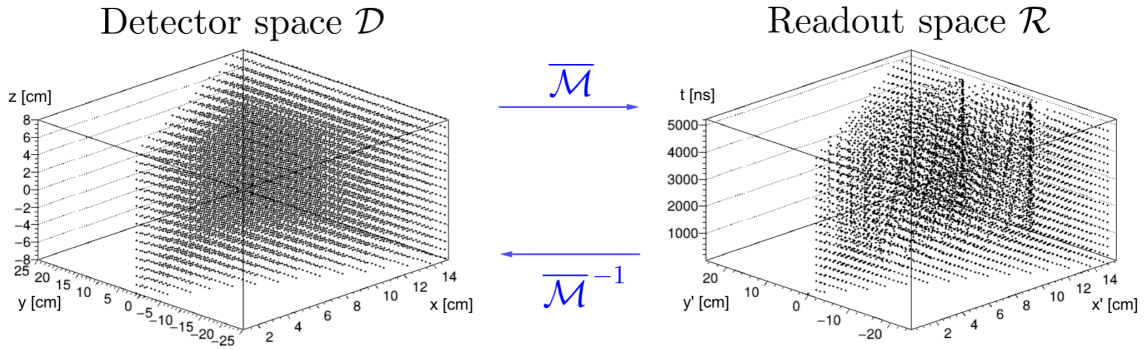


Figure 7: A visualization of the direct mapping \mathcal{M} between the detector coordinate space and the corresponding readout coordinate space and of its inverse \mathcal{M}^{-1} .

the point we want to map, effectively forming a pseudocube around it. Due to the uneven spacing of these points (see the right part of Fig. 7 with the resulting grid in the readout coordinate system), we can no longer use trilinear interpolation to find the resulting point in the detector space. Instead, we use a similar interpolation method, which includes the determination of the coefficients of a polynomial

$$f(x', y', t) = ax'y't + bx'y' + cx't + dy't + ex' + fy' + gt + h$$

for each of the reconstructed coordinates $\tilde{x}, \tilde{y}, \tilde{z}$ in the detector space based on the surrounding points.

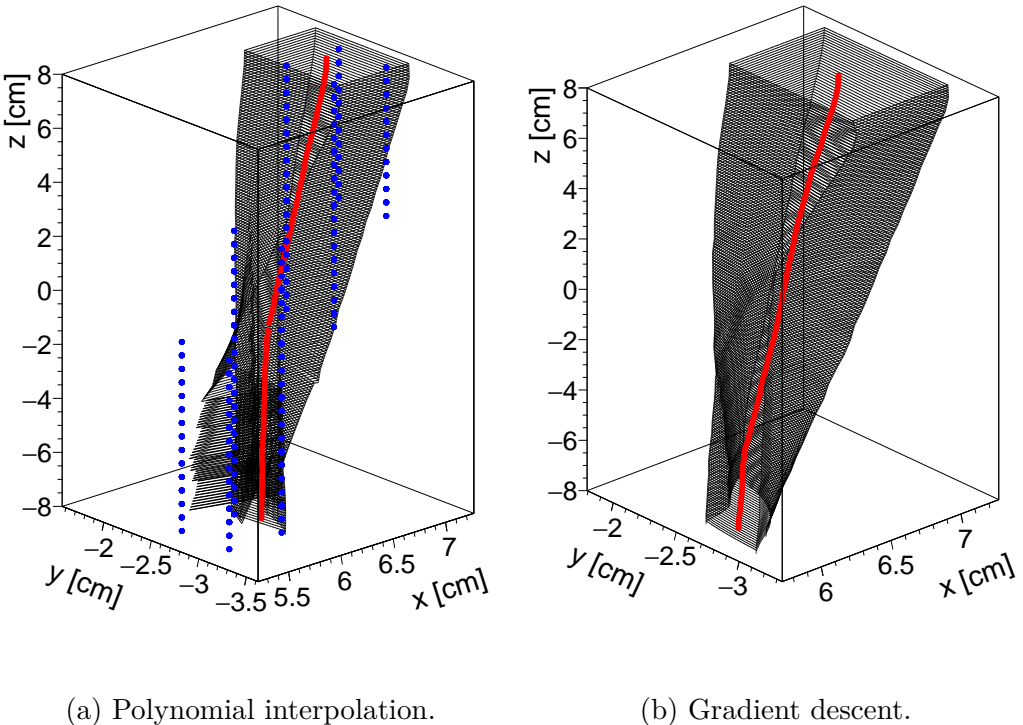


Figure 8: Comparison of the reconstruction of boundaries of the problematic pad 12 near the magnet pole for different drift times (time step 100 ns) using the two methods of \bar{M} inversion. The reconstructed centers of the pad and time bin are denoted by red points, and the simulated map points used for the interpolation are in blue. Polynomial interpolation in this region with high distortion leads to unwanted artifacts for large drift paths (spikes in the black boundaries, less significant effect on the red centers). Only ten corner pads are affected (8 of them near the vacuum tube), and in current simulations, electrons in these regions are very rare.

3.2 Simulation and reconstruction of primary tracks

To develop and test the reconstruction procedure, a simulation of the primary tracks is needed. The movement of primary particles, together with the production of secondaries in the primary vertices, was simulated using the HEED program (High Energy Electro-Dynamics) [25], which is part of the Garfield++ toolkit.

The response of the OFTPC to primary tracks with different initial parameters, forming a regular grid that covers the kinematic phase space of tracks, was simulated on the MetaCentrum computer grid (see Acknowledgments). In the case of beryllium, the grid was chosen, based on expected/needed resolutions, to have 21 points in θ range $[-17.1^\circ, 17.1^\circ]$, 21 points in ϕ range $[-16.3^\circ, 16.3^\circ]$, and 11 points in the energy E_{in} range [3, 13] MeV, both for electron and positron primary tracks. An example of

a simulated track is shown in Fig. 9; the primary track is drawn in black, and the secondary electrons, drifting and diffusing towards the readout, in orange.

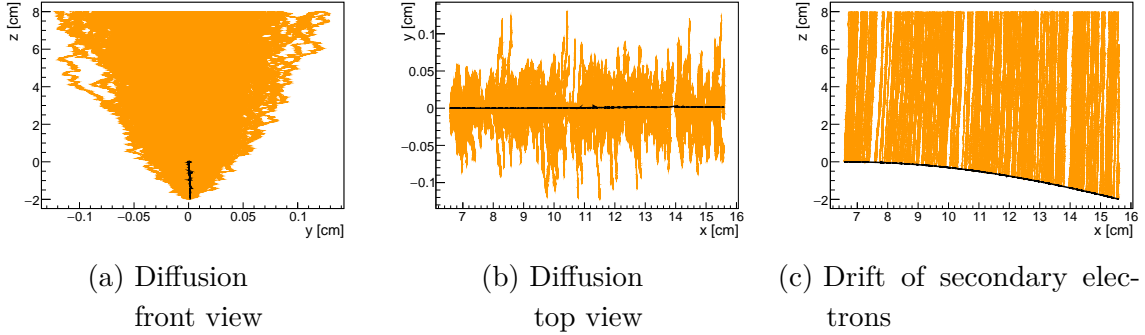


Figure 9: Simulation showing a track of a primary particle (drawn in black) and corresponding tracks of secondaries (drawn in orange). The projections shown in figures (a) and (b) demonstrate randomness of the process, which is why the average direct $\bar{\mathcal{M}}$, Eq. 3.1, and inverse $\bar{\mathcal{M}}^{-1}$, Eq. 3.2, mappings are used.

To study the limitations of the reconstruction procedure, we first consider an idealized, *continuous* readout plane. For the secondary electrons produced by a (simulated) primary track (x_i, y_i, z_i) the corresponding reconstructed vertices $(\tilde{x}_i, \tilde{y}_i, \tilde{z}_i)$ are found by applying $\bar{\mathcal{M}}^{-1}$ on the readout positions, see the example in Fig. 10. The z -coordinates of the vertices are reconstructed based on the time information, whose measurement starts when the primary track triggers the detector. Here, it happens when a particle enters the OFTPC volume; in reality, we expect it will be triggered by the MWPC detector. As it only takes about 0.5 ns from the creation of a primary particle to its exit from the entire detector, this difference is negligible, even compared to the fluctuation of the drift time.

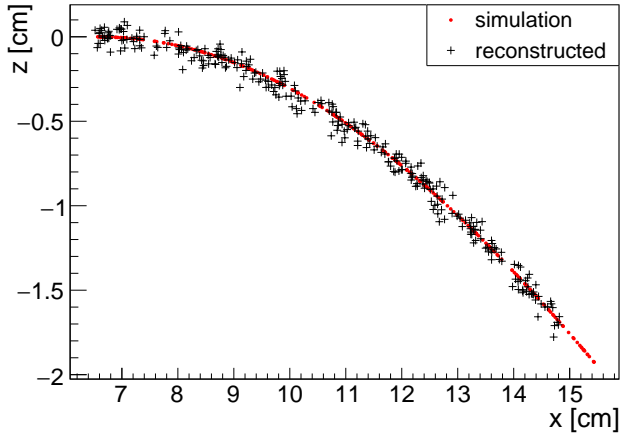


Figure 10: Simulated (in red color) and reconstructed interaction points for the simulated primary track with the kinetic energy of 8 MeV electron entering into the OFTPC at the position $(6.51, 0, 0)$ cm (which corresponds to the center of the window of the OFTPC) and having direction vector $(1, 0, 0)$.

The histograms of the residuals are summarized in Fig. 11. The errors are caused by the diffusion of drifting ionization electrons resulting from their random collisions with gas particles (an effect that the map cannot account for; see, for example, Fig. 9). We also see a small systematic shift in z , which might be caused by the non-zero initial velocities of the ionization electrons (not considered when simulating the map).

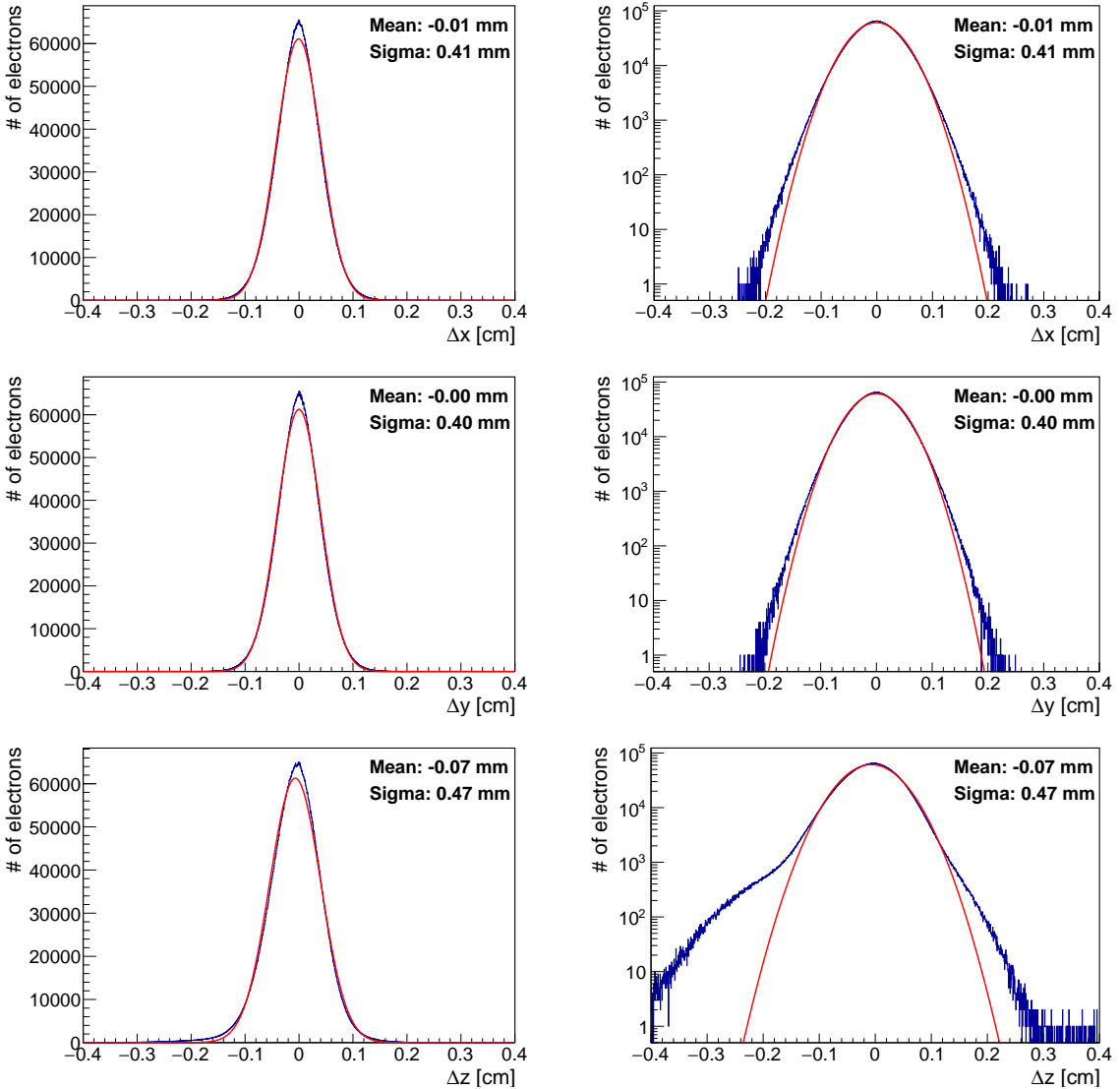


Figure 11: Gaussian fit of x , y , and z residuals of reconstructed vertex coordinates, i.e., differences of original and reconstructed vertices $(x, y, z) - (\tilde{x}, \tilde{y}, \tilde{z})$. Histograms in linear (left) and logarithmic (right) scales are shown. Data from 14 277 175 electrons from 48 485 simulated tracks were used. The statistical uncertainty of the original histograms is very small and is omitted. From a shape point of view, the fits do not fit the data perfectly. More plots to see the dependence on the tracks' parameters would be interesting. - sure, but let's postpone it to another step.

In reality, the readout plane is divided into pads, as shown in Fig. 12. The charge collected by each pad is assigned to its center and to the center of the time bin, which means a less dense domain of the inverse map $\overline{\mathcal{M}}^{-1}$ used for track reconstruction. In the future, this approach might be refined using a likelihood method. We can

precalculate the map for these points if the reconstruction speed becomes an issue.

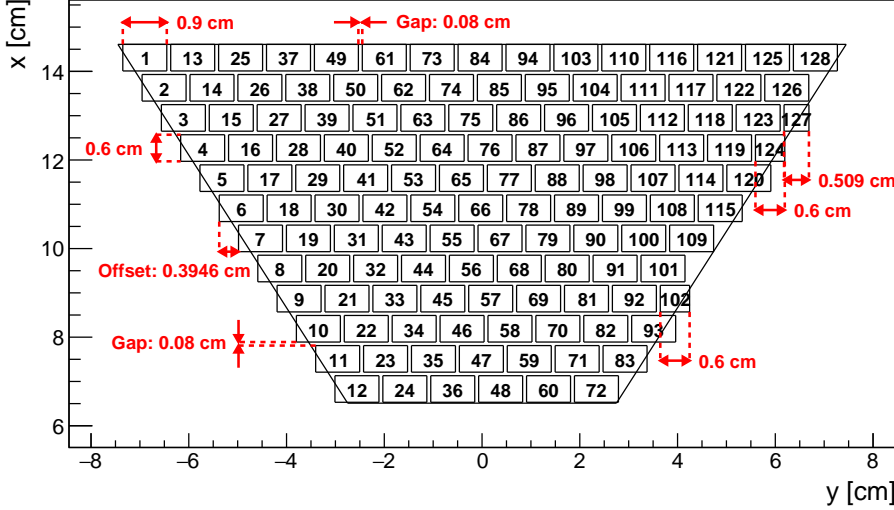


Figure 12: Pad layout of one of the OFTPC readout planes and its parameters. Pads 102, 124, and 127 are irregular; the rest have the same dimensions.

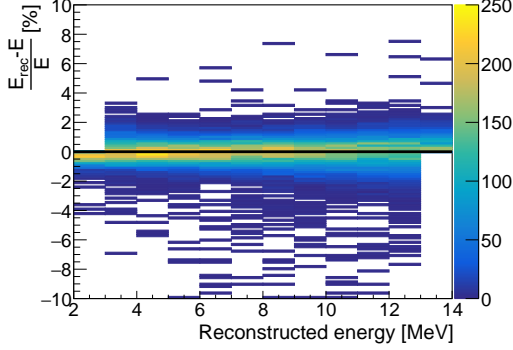
The multiplying effect of the GEM foil is not accounted for⁴, and for the reconstruction procedure, all pads are considered to have the same area, although there are three special pads near the detector edge. Using the inverse map $\overline{\mathcal{M}}^{-1}$ in the centers of each hit pad/time bin, the reconstructed voxels of the primary track are found, and a weight equal to the number of ionization electrons is assigned to each of them.

3.3 Energy reconstruction

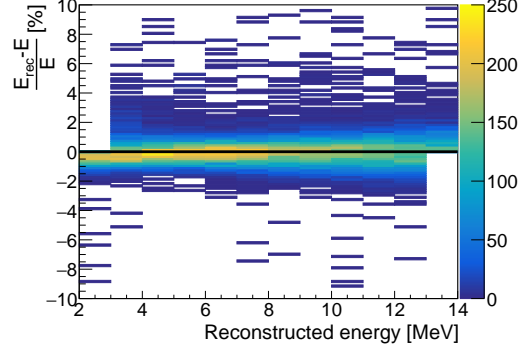
The track passing the reconstructed vertices is determined by the MIGRAD minimization algorithm implemented in ROOT [26]. The minimized function has the standard form of the weighted sum of squares of the differences between the reconstructed positions of the primary vertices and the corresponding vertices of the single variable — particle energy. The parameterized track is calculated by the Runge-Kutta algorithm using as the input (a) the direction vector of the track (spherical angles θ and φ), (b) the track origin in the TPC window (y_0, z_0) and (c) the description, via a grid of points, of a nontrivial magnetic field within the OFTPC volume. Using the Runge-Kutta algorithm, a trajectory is calculated in the nontrivial magnetic field of the OFTPC.

The results are summarized as functions of track parameters: reconstructed energy E_{rec} , polar θ and azimuthal φ angles, for the segmented readout plane, in Figs. 13e-13f. Systematic errors were corrected using a 3D linear fit.

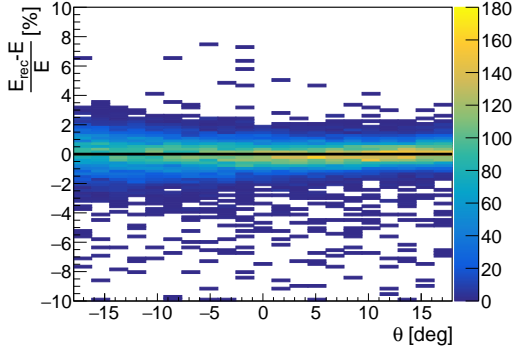
⁴The GEMs might affect the resolution of energy reconstruction due to a) their gain fluctuation (which can lower the energy resolution) and b) charge spreading/sharing (which can improve the energy resolution).



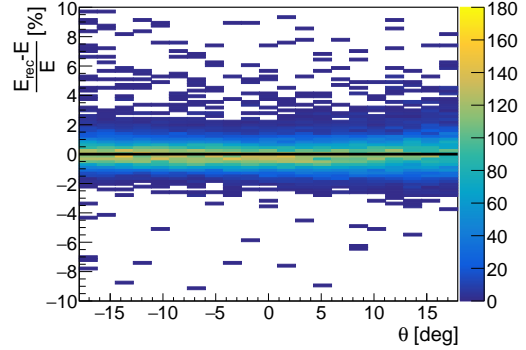
(a) Reconstructed energy accuracy as a function of reconstructed energy E_{rec} for primary electrons.



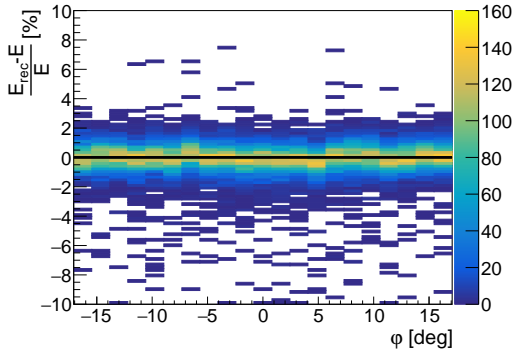
(b) Reconstructed energy accuracy as a function of reconstructed energy E_{rec} for primary positrons.



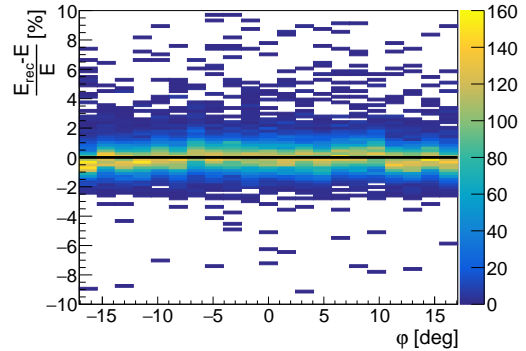
(c) Reconstructed energy accuracy as a function of simulated polar angle θ for primary electrons.



(d) Reconstructed energy accuracy as a function of simulated polar angle θ for primary positrons.



(e) Reconstructed energy accuracy as a function of simulated azimuthal angle φ for primary electrons.



(f) energy resolution as a function of azimuthal angle φ for primary positrons

Figure 13: Accuracy of reconstructed energy, both for electrons (in the left column) and positrons (in the right column) as a function of reconstructed energy (the upper line), polar angle θ (the middle line), and azimuthal angle φ (the bottom line).

The result of reconstructed energy resolution, without details about its energy and angular dependencies, is plotted in Fig. 14,

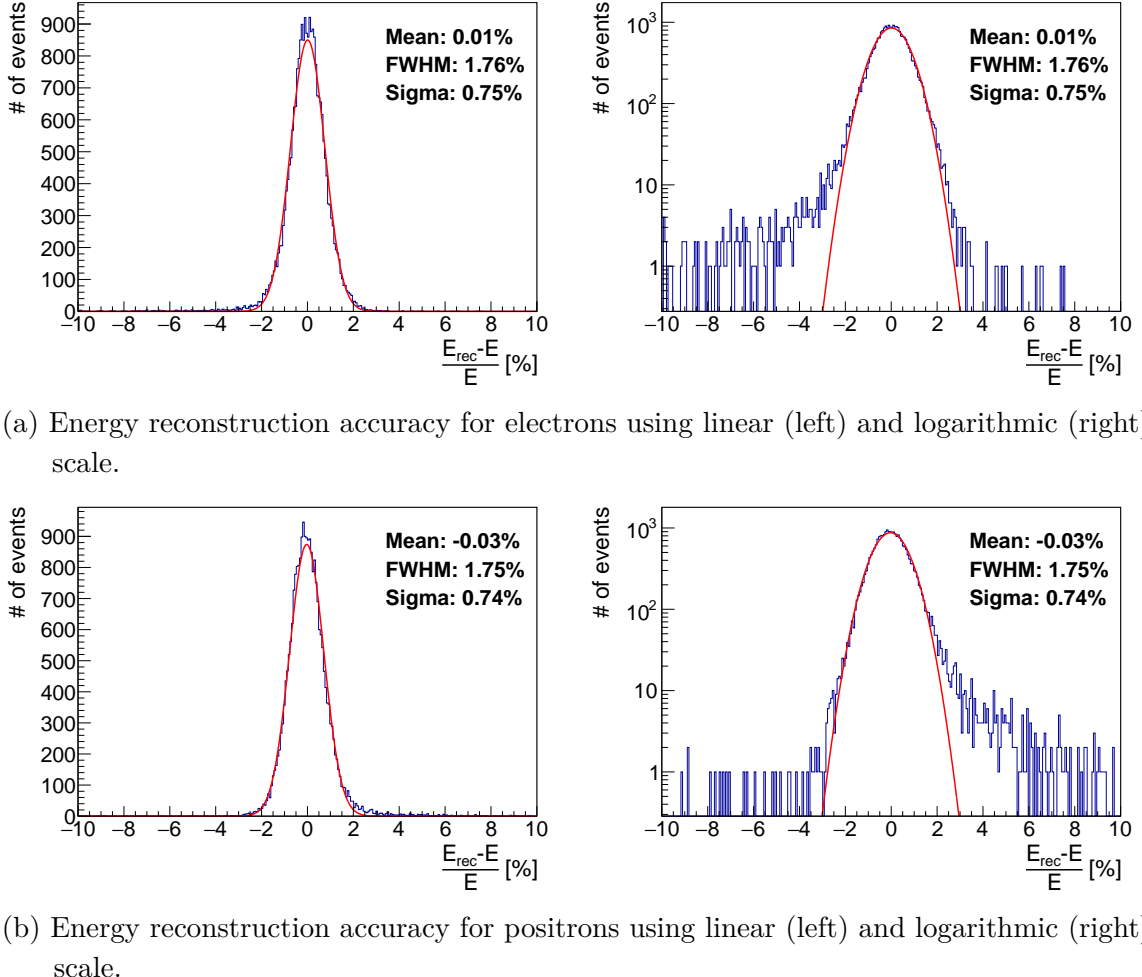


Figure 14: Algorithm energy reconstruction accuracy. The sigma values are taken from the Gaussian fit. This makes them lower compared to direct calculation via RMS ($1\% \rightarrow 0.75\%$) because of outliers.

and it shows that the relative systematic uncertainty of energy reconstruction is better than 1% both for electrons and positrons.

4 Update of 2D histogram of pair angle vs positron energy - angular uncertainty

The uncertainty in the energy reconstruction determined in the previous section can be complemented with the uncertainty of θ_{+-} and included in Fig. 2 to get a closer distribution to the one expected from the real measurements.

A simple (and rough) estimate of the accuracy of a single particle direction vector, based on a purely geometric consideration, is

$$\frac{1}{2} \arccos \left(\frac{d^2 - 2(d_{\text{TPX3}} + r_{\text{TAR}})^2}{d^2 + 2(d_{\text{TPX3}} + r_{\text{TAR}})^2} \right) \quad (4.1)$$

where d_{TPX3} and r_{TAR} are the size of the TPX3 detector pixel and radius of the target, respectively, and d is the shortest distance between the TPX3 detector and the center of the target. For values $d_{\text{TPX3}} = 50 \mu\text{m}$, $r_{\text{TAR}} = 1000 \mu\text{m}$ and $d = 18000 \mu\text{m}$ the maximal angular uncertainty is less than 5° which, on average, gives a resolution better than $5^\circ/\sqrt{12} \approx 1.4^\circ$. The combined uncertainty of the angle between the two particles is then better than 3° .

However, there is a much larger effect contributing to the angular uncertainty than the finite pixelation of the TPX3 detector — multiple scattering due to the passage of the particle through the material surrounding the target and the material of the TPX3 itself. The result, based on the detector full simulation, including signal formation in TPX3 and its pixelization, is shown in Fig. 15:

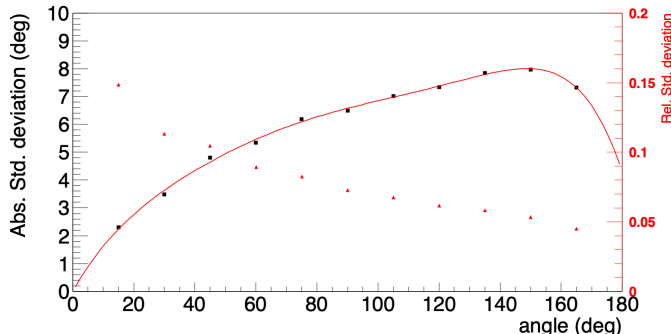


Figure 15: Absolute and relative standard deviations of the reconstructed correlation angle θ_{+-} in the TPX3 detector layer are shown as functions of the true correlation angle. Although these results correspond to the *triangular* rather than the hexagonal TPX configuration, we can use them as a conservative estimate. The dominant contribution to the angular uncertainty arises from material effects, which are larger in the triangular configuration due to the longer particle paths through its corner regions.

5 Discussion of results and conclusion

By combining the results for the energy-reconstruction precision (Fig. 14) and the angular resolution (Fig. 15), the idealized case shown in Fig. 2 is modified as depicted in Fig. 16. Nonetheless, even after accounting for detector effects that smear the original distribution, the X17 signal remains clearly distinguishable.

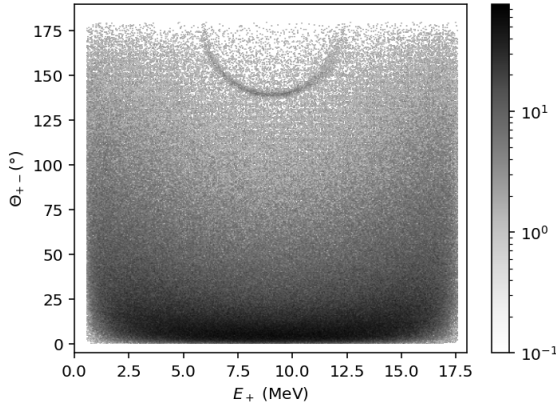


Figure 16: 2D histogram of e^+e^- angle vs positron energy of pairs created in the standard Internal Pair Creation process, and pairs created by the decay of a hypothetical boson X17 as expected to be seen in a real measurement. Although the gap separating the background from the decay production is not as pronounced as in Figure 2, the separation is clear. The data used for the plot originates from a simulation combined with the limits due to the detector construction and reconstruction procedure, influencing the precision of both the angles and energies. 10^6 events were used to generate the plot, representing the estimated lower limit of the number of measured events. The branching ratio $X17/IPC$ equal to 3×10^{-3} was used.

The achieved (conservative) accuracies of the relative energy reconstruction—RMS better than 1% (1.8%) for both electrons and positrons—are very promising and surpass typical performance levels obtained with standard TPCs in the HEP domain [15].

We note, however, that the presented results do not account for several important factors: a) the real magnetic-field map may differ from the one used in the reconstruction, and b) the direction vectors of the primary tracks are known only with limited precision. Both effects can influence the uncertainty of the reconstructed energy. Moreover, the impact of the GEM is not yet known, and the precision of the trigger timing also plays a role—unlike in a conventional TPC, where shifting the entire trajectory in time does not change the magnetic field experienced along it and therefore does not affect the reconstructed energy.

On the positive side, the effect of imperfect knowledge of the magnetic field can be mitigated by measuring it directly, for example using probes or dedicated laser/muon tracks.

I don't like such huge captions. The background information needed to understand it is so much that whatever you write here is not enough and makes it confusing...

CRediT author statement

Martin Vavřík: Methodology, Software, Analysis, Investigation, Visualization.
Babar Ali: Writing - Review & Editing. **Hugo Natal da Luz:** Conceptualization, Investigation, Software, Formal Analysis, Validation, Supervision, Project Administration. **Olivier Rousselle:** Software, Analysis, Investigation, Visualization. **Rudolf Sýkora:** Writing - Review & Editing, Investigation. **Tomáš Sýkora:** Conceptualization, Supervision, Writing – Original Draft Preparation, Validation, Investigation.

Acknowledgments

This work was supported by the GAČR - Czech Science Foundation grant GA21-21801S. Computational resources, MetaCentrum, were provided by the e-INFRA CZ project (ID:90140), supported by the Ministry of Education, Youth and Sports of the Czech Republic (MEYS). The measurements with the proton beam took place in the Van de Graaff accelerator laboratory, supported by the LM2018108 grant of MEYS. As per non-commercial license agreement: Made with GeoGebra® ([Figure 5](#))

References

- [1] A. J. Krasznahorkay et al. *Phys. Rev. Lett.* **116** (2016), no. 4 042501, [[arXiv:1504.01527](#)].
- [2] M. Rose *Phys. Rev.* **76** (1949) 678–681. [Erratum: Phys.Rev. 78, 184–184 (1950)].
- [3] A. Krasznahorkay et al. [arXiv:1910.10459](#).
- [4] A. J. Krasznahorkay et al. [arXiv:2209.10795](#).
- [5] A. J. Krasznahorkay, A. Krasznahorkay, M. Csatlós, J. Timár, M. Begala, A. Krakó, I. Rajta, I. Vajda, and N. J. Sas *Universe* **10** (2024), no. 11.
- [6] D. Barducci and C. Toni *Journal of High Energy Physics* **2023** (feb, 2023).
- [7] D. S. Alves, D. Barducci, G. Cavoto, L. Darmé, L. Delle Rose, L. Doria, J. L. Feng, A. Frankenthal, A. Gasparian, E. Goudzovski, and et al. *The European Physical Journal C* **83** (2023), no. 3 230.
- [8] “52nd International Symposium on Multiparticle Dynamics.” <https://garfieldpp.web.cern.ch/garfieldpp/>. Accessed: 2023-12-18.
- [9] T. T. Anh, T. Dinh Trong, A. J. Krasznahorkay, A. Krasznahorkay, J. Molnár, Z. Pintye, N. A. Viet, N. T. Nghia, D. T. Khanh Linh, B. T. Hoa, L. X. Chung, and N. T. Anh *Universe* **10** (Apr., 2024) 168.
- [10] K. U. Abraamyan, C. Austin, M. I. Baznat, K. K. Gudima, M. A. Kozhin, S. G. Reznikov, and A. S. Sorin, *Observation of structures at 17 and 38 MeV/c² in the γγ*

invariant mass spectra in pC, dC, and dCu collisions at p_{lab} of a few GeV/c per nucleon, 2023.

- [11] T. M. I. collaboration, K. Afanaciev, A. M. Baldini, S. Ban, H. Benmansour, G. Boca, P. W. Cattaneo, G. Cavoto, F. Cei, M. Chiappini, A. Corvaglia, G. D. Maso, A. D. Bari, M. D. Gerone, L. F. Barusso, M. Francesconi, L. Galli, G. Gallucci, F. Gatti, L. Gerritzen, F. Grancagnolo, E. G. Grandoni, M. Grassi, D. N. Grigoriev, M. Hildebrandt, F. Ignatov, F. Ikeda, T. Iwamoto, S. Karpov, P. R. Kettle, N. Khomutov, A. Kolesnikov, N. Kravchuk, V. Krylov, N. Kuchinskiy, F. Leonetti, W. Li, V. Malyshev, A. Matsushita, M. Meucci, S. Mihara, W. Molzon, T. Mori, D. Nicolò, H. Nishiguchi, A. Ochi, W. Ootani, A. Oya, D. Palo, M. Panareo, A. Papa, V. Pettinacci, A. Popov, F. Renga, S. Ritt, M. Rossella, A. R. S. Scarpellini, P. Schwendimann, G. Signorelli, M. Takahashi, Y. Uchiyama, A. Venturini, B. Vitali, C. Voena, K. Yamamoto, R. Yokota, and T. Yonemoto, *Search for the X17 particle in ${}^7\text{Li}(\text{p}, \text{e}^+\text{e}^-){}^8\text{Be}$ processes with the MEG II detector*, 2024.
- [12] “The laboratory of the Van de Graaff accelerator.”
<http://aladdin.utef.cvut.cz/projekty/vdg/>. Accessed: 2023-05-12.
- [13] B. Ali, Z. Kohout, H. N. da Luz, O. Rousselle, R. Sýkora, and T. Sýkora *Radiation Measurements* **184** (2025) 107424.
- [14] M. V. Vavřík, *Simulation and Reconstruction of Charged Particle Trajectories in an Atypic Time Projection Chamber*. bachelor thesis, Faculty of Mathematics and Physics, 2025.
- [15] H. J. Hilke *Reports on Progress in Physics* **73** (oct, 2010) 116201.
- [16] W. Blum, L. Rolandi, and W. Riegler, *Particle detection with drift chambers*. Particle Acceleration and Detection. 2008.
- [17] D. Adamová, G. Agakichiev, D. Antończyk, H. Appelshäuser, V. Belaga, J. Bielčíková, P. Braun-Munzinger, R. Campagnolo, A. Cherlin, S. Damjanović, T. Dietel, L. Dietrich, A. Drees, W. Dubitzky, S. Esumi, K. Filimonov, Z. Fraenkel, C. Garabatos, P. Glässel, G. Hering, J. Holeczek, V. Kushpil, A. Marín, J. Milošević, A. Milov, D. Miśkowiec, L. Musa, Y. Panebrattsev, O. Pechenova, V. Petráček, A. Pfeiffer, J. Rak, I. Ravinovich, M. Richter, H. Sako, E. Schäfer, W. Schmitz, J. Schukraft, W. Seipp, A. Sharma, S. Shimansky, J. Stachel, M. Šumbera, H. Tilsner, I. Tserruya, J. Wessels, T. Wienold, B. Windelband, J. Wurm, W. Xie, S. Yurevich, and V. Yurevich *Nuclear Instruments and Methods in Physics Research Section A: Accelerators, Spectrometers, Detectors and Associated Equipment* **593** (Aug., 2008) 203–231.
- [18] I. Albayrak, S. Aune, C. A. Gayoso, P. Baron, S. Bültmann, G. Charles, M. Christy, G. Dodge, N. Dzbenksi, R. Dupré, K. Griffioen, M. Hattawy, Y. Hung, N. Kalantarians, S. Kuhn, I. Mandjavidze, A. Nadeeshani, M. Ouillon, P. Pandey, D. Payette, M. Pokhrel, J. Poudel, A. Tadepalli, and M. Vandenbroucke *Nuclear Instruments and Methods in Physics Research Section A: Accelerators, Spectrometers, Detectors and Associated Equipment* **1062** (2024) 169190.

- [19] *Design of a Radial TPC for Antihydrogen Gravity Measurement with ALPHA-g.*
<https://journals.jps.jp/doi/pdf/10.7566/JPSCP.18.011015>.
- [20] F. Collaboration, A. Ariga, T. Ariga, J. Boyd, F. Cadoux, D. W. Casper, F. Cerutti, S. Danzeca, L. Dougherty, Y. Favre, J. L. Feng, D. Ferrere, J. Gall, I. Galon, S. Gonzalez-Sevilla, S.-C. Hsu, G. Iacobucci, E. Kajomovitz, F. Kling, S. Kuehn, M. Lamont, L. Levinson, H. Otono, J. Osborne, B. Petersen, O. Sato, M. Sabate-Gilarte, M. Schott, A. Sfyrla, J. Smolinsky, A. M. Soffa, Y. Takubo, P. Thonet, E. Torrence, S. Trojanowski, and G. Zhang, *Technical Proposal for FASER: ForwArd Search ExpeRiment at the LHC*, 2018.
- [21] A. Cortez, H. N. da Luz, R. Sýkora, B. Ali, and L. Fajt *Nuclear Instruments and Methods in Physics Research Section A: Accelerators, Spectrometers, Detectors and Associated Equipment* **1047** (2023) 167858.
- [22] “Garfield++.” <https://garfieldpp.web.cern.ch/garfieldpp/>. Accessed: 2023-05-18.
- [23] K. V. MARDIA *Biometrika* **57** (12, 1970) 519–530,
[\[https://academic.oup.com/biomet/article-pdf/57/3/519/702615/57-3-519.pdf\]](https://academic.oup.com/biomet/article-pdf/57/3/519/702615/57-3-519.pdf).
- [24] Wikipedia contributors, *Binary search algorithm — Wikipedia, The Free Encyclopedia*, 2023. [Online; accessed 21-December-2023].
- [25] I. Smirnov *Nuclear Instruments and Methods in Physics Research Section A: Accelerators, Spectrometers, Detectors and Associated Equipment* **554** (2005), no. 1 474–493.
- [26] R. Brun and F. Rademakers *Nucl. Instrum. Meth. A* **389** (1997) 81–86.